Langmuir

Article

pubs.acs.org/Langmuir

Dispersion Stability of Functionalized Graphene in Aqueous Sodium Dodecyl Sulfate Solutions

Andrew G. Hsieh,[†] Sibel Korkut,[†,‡] Christian Punckt,[†,‡] and Ilhan A. Aksay*[,†]

[†]Department of Chemical and Biological Engineering, Princeton University, Princeton, New Jersey 08544, United States

[‡]Vorbeck Princeton Research Center, Vorbeck Materials Corp., 11 Deerpark Drive, Monmouth Junction, New Jersey 08852, United States

Supporting Information

ABSTRACT: The colloidal stability of functionalized graphene sheets (FGSs) in aqueous sodium dodecyl sulfate (SDS) solutions of different concentrations was studied by optical microscopy and ultraviolet−visible light absorption after first dispersing the FGSs ultrasonically. In up to ∼10 μM SDS solutions, FGSs reaggregated within a few minutes, forming ramified structures in the absence of SDS and increasingly compact structures as the amount of SDS increased. Above ∼10 μM, the rate of reaggregation decreased with increasing SDS concentration; above ∼40 μM, the suspensions were colloidally stable for over a year. The concentration of ∼40 μM SDS lies 2 orders of magnitude below the critical surface aggregation concentration of ∼1.8 mM SDS on FGSs but above the concentration (∼18 μM) at which SDS begins to form a monolayer on FGSs. Neither surface micelle nor dense monolayer coverage is therefore required to obtain stable aqueous FGS dispersions. We support our experimental results by calculating the van der Waals and electrostatic interaction energies between FGSs as a function of SDS concentration and show that the experimentally observed transition from an unstable to a stable dispersion correlates with a transition from negative to positive interaction energies between FGSs in the aggregated state. Furthermore, our calculations support experimental evidence that aggregates tend to develop a compact structure over time.

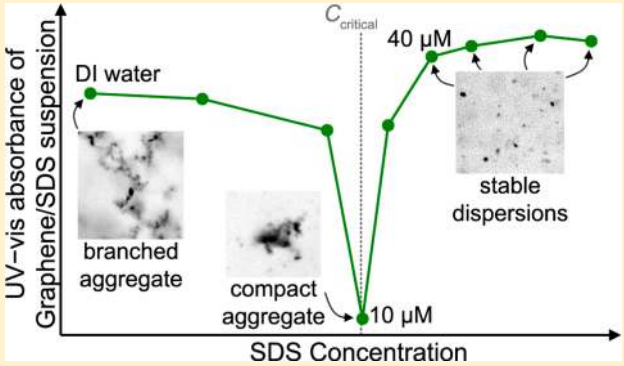

INTRODUCTION

Functionalized graphene sheets (FGSs) can be produced in large quantities by simultaneous thermal exfoliation and reduction of graphite oxide (GO)[1,2] or by chemical reduction of graphene oxide[3] and have been used in a wide variety of applications due to their extraordinary physical properties: In lithium ion batteries, for example, the inclusion of electrically conducting FGSs in metal oxide electrodes increases power density.[4−7] In polymer composites, the presence of FGSs leads to higher modulus,[8−10] elongation at failure,[8,10] and strength[8−10] while improving the thermal stability[8,11] and providing electrical conductivity as well.[9,10,12] When added to liquid fuels, FGSs may lower ignition temperatures and enhance combustion rates.[13,14] The benefit of FGSs in these applications stems from interactions of the metal oxide, polymer matrix, or fuel molecules with graphene and, in particular, with the lattice defects (topological defects and vacancies)[1,15] and oxygen-containing functional groups[1,15] found on FGSs. As such, to take full advantage of the properties of FGSs, their accessible surface area needs to be maximized.

The theoretical specific surface area of graphene is 2630 m^2/g. However, in dry FGS powders obtained from the thermal reduction of GO, the restacking of the sheets decreases the surface area to 500−700 m^2/g, as determined by nitrogen adsorption.[2] Loosely aggregated FGSs can be separated from one another with sufficient energy input, for example via ultrasonication in a solvent,[1,2] and can be dispersed into mostly individual sheets, leading to an accessible surface area of up to 1850 m^2/g in suspension.[2] However, FGSs reaggregate due to attractive van der Waals forces once the energy input from ultrasonication ceases, unless reaggregation is prevented either by reducing the van der Waals forces through refractive index matching[16] or by introducing repulsive steric, electrostatic, or electrosteric forces. FGSs that are dispersed in polar aprotic solvents such as *N*-methyl-2-pyrrolidone or dimethylformamide typically form suspensions that are stable over a time scale of months,[17,18] likely due to refractive index matching between FGSs and the solvent.[16] Nevertheless, aqueous FGS suspensions are necessary for many practical applications, such as graphene−metal oxide nanocomposites for battery electrodes,[4,6] graphene−polymer composites,[8,9] and high surface area tapes.[19] This generates a demand for aqueous FGS suspensions that are stable over the time scales of the respective processes.

Received: September 12, 2013
Revised: November 1, 2013

   dx.doi.org/10.1021/la4035326 | *Langmuir* XXXX, XXX, XXX−XXX

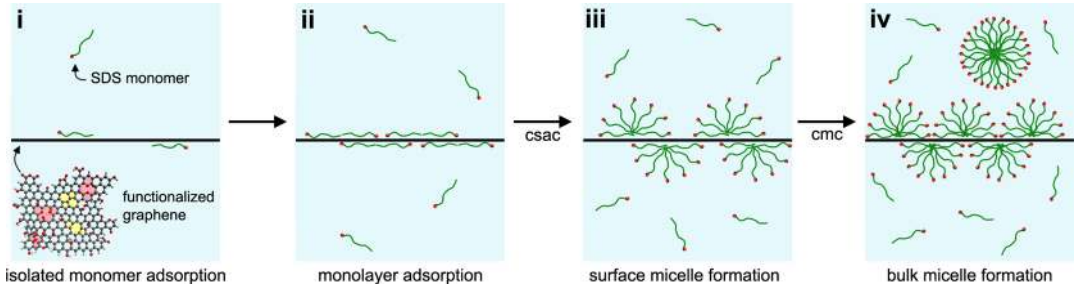

Figure 1. Schematic representation of the four stages of SDS adsorption onto functionalized graphene: (i) adsorption of isolated surfactant monomers, (ii) adsorption of a surfactant monolayer, (iii) formation of hemi-cylindrical surface micelles, and (iv) formation of micelles in bulk solution. Also indicated are the critical surface aggregation concentration (csac) and the critical micelle concentration (cmc). The functionalized graphene schematic shows oxygen functionalities (red), 5−8−5 and 5−7−7−5 topological defects (yellow), and lattice vacancies (pink).

Due to the large mismatch in the refractive indices of water[20] and FGSs,[21] the introduction of repulsive electrostatic or steric interactions is necessary to obtain stable dispersions.

FGSs exhibit a high number density of oxygen-containing functional groups.[1,15] As a result, electrostatic stabilization in water can be achieved by increasing the suspension pH above the pK_a of acidic groups such as carboxyls or phenolic hydroxyls,[1,15,22,23] which results in deprotonation and leaves a negative charge on the sheets.[23,24] In cases where pH adjustment is not feasible or where there is an insufficient number density of functional groups on the graphene, the preparation of aqueous FGS suspensions typically involves the use of surfactant solutions, as adsorbed surfactant molecules can provide steric or (for ionic surfactants) electrostatic repulsion between the individual FGSs. With this goal in mind, we recently examined the adsorption behavior of the ionic surfactant sodium dodecyl sulfate (SDS) on FGSs using conductometric titration, a technique which is unique in its ability to sample a broad range of surfactant concentrations with high resolution.[25] Our findings were consistent with a four-stage adsorption model, shown schematically in Figure 1: (i) the adsorption of isolated surfactant monomers with their alkyl chains oriented parallel to the surface, (ii) the subsequent formation of a surfactant monolayer (alkyl chains still oriented parallel to the surface), (iii) the formation of hemi-cylindrical surface micelles prior to micelle formation in the bulk solution, and (iv) the formation of micelles in bulk solution. We determined the SDS concentration at which a dense monolayer forms on FGSs, the SDS concentration at the onset of surface micelle formation on FGSs, known as the critical surface aggregation concentration (csac), and the onset of micelle formation in the bulk solution, known as the critical micelle concentration (cmc).

The stability of FGSs dispersed in aqueous surfactant solutions is influenced by the amount, charge, and morphology of the adsorbed surfactant, but so far the relation between surfactant adsorption and colloidal stability has not been systematically explored for FGSs. Such studies have been carried out for graphitic particles dispersed in aqueous surfactant solutions; it has been demonstrated that concentrations greater than the csac are required to achieve aqueous suspensions that are stable on the time scale of about a day.[26,27] Furthermore, while there are a number of studies on surfactant-assisted dispersions of graphene in water,[28−32] the current literature does not link dispersion stability to the adsorption behavior of surfactants on graphene.

In this contribution, we build upon our recent conductometric titration study of SDS/FGS aqueous dispersions[25] by relating the SDS adsorption behavior directly to the colloidal stability of FGSs in water. Specifically, we examine the aggregate morphology, settling behavior, and reaggregation rate of FGSs with optical microscopy and ultraviolet−visible (UV−vis) absorbance measurements. By calculating the interaction energy between FGSs as a function of SDS concentration, we also demonstrate how SDS adsorption influences the reaggregation behavior and dispersion stability of FGSs. Contrary to previous studies with graphitic carbon particles, we find that SDS concentrations 2 orders of magnitude lower than the csac are sufficient to achieve colloidal stability.

METHODS

Production of FGSs. Graphite oxide (GO) was prepared according to the Staudenmaier method,[33] as detailed elsewhere, using graphite powder sized at ∼45 μm (grade 230, Asbury Carbons).[1,2] The GO was placed at the bottom of a fused silica tube (Technical Glass Products) and dried overnight under flowing nitrogen. The tube was evacuated and purged with ultrahigh-purity argon (Air Products) three times. The tube was evacuated once more and, while GO was still under vacuum, thermal reduction and exfoliation of GO were simultaneously carried out by placing the tube in a three-zone tube furnace (Lindberg/Blue M, SPX Thermal Product Solutions), set to a temperature of 1100 °C, for 60 s. The as-produced FGS powder had a surface area of ∼690 m^2/g, as determined from nitrogen adsorption (Gemini V, Micrometrics Instruments Corporation) by the Brunauer, Emmett, and Teller (BET) method.[34] The molar carbon-to-oxygen ratio (C/O) of the FGSs was ∼18, measured by energy dispersive X-ray spectroscopy (INCA x-act, Oxford Instruments, attached to a Vega 1 scanning electron microscope, Tescan USA).

Dispersion of FGSs in Aqueous SDS Solutions. SDS solutions were prepared by dissolving SDS (≥ 99% purity, used as-received, Sigma Aldrich) in deionized (DI) water (Picopure 2 UV Plus system, Hydro Service and Supplies, Inc.) at concentrations ranging from 0 to 10 mM. This range includes the concentration at which SDS forms an adsorbed monolayer at full surface coverage on FGSs (∼18 μM),[25] the csac for SDS on FGSs (∼1.8 mM),[25] and the cmc of SDS in water (∼8.1 mM).[35−37] To 50 mL of each SDS solution, we added 5 mg of FGSs and performed ultrasonication at ∼300 W (VCX 750 ultrasonic processor unit, Sonics & Materials, Inc.) for 1 h while cooling the mixture in an ice bath. One sample was prepared at each SDS concentration.

After sonication, an aliquot of each sample was diluted 1:9 with an SDS solution of the same concentration as present in the sample, and its transmittance was measured at 400 nm with UV−vis spectroscopy (Evolution 300 spectrometer, Thermo Scientific) to determine the concentration of FGSs in suspension.[38] We neglect scattering effects and assume that the optical properties of FGSs in suspension are independent of sheet size as well as aggregate size and morphology. As

dx.doi.org/10.1021/la4035326 | Langmuir XXXX, XXX, XXX−XXX

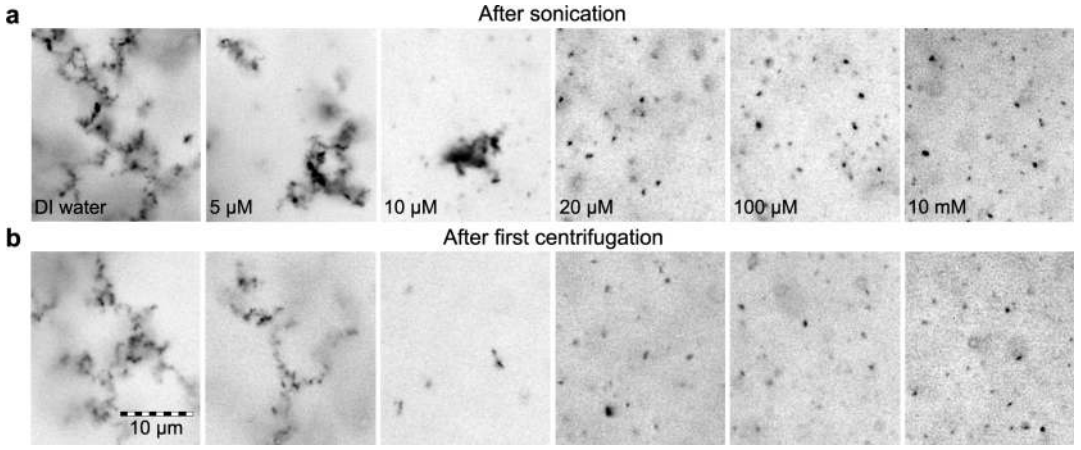

Figure 2. Representative optical microscope images of FGSs dispersed at a concentration of 0.1 mg/mL in aqueous SDS solutions (a) after sonication and (b) after the first centrifugation (1 h later); [SDS] in each sample (from left to right): 0 μM (DI water), 5 μM, 10 μM, 20 μM, 100 μM, and 10 mM; the scale bar is the same for all images.

dispersions of pristine graphene display a linear relationship between concentration and absorbance according to the Beer–Lambert law,[38] herein we report sample absorbance, which we assume to be proportional to FGS concentration. The state of FGS aggregation in each sample was determined with optical microscopy imaging (Axioplan 2, Carl Zeiss Microscopy) using a water immersion objective (C-Apochromat 63×/1.2 W Korr, Carl Zeiss Microscopy). To accomplish this, a poly(dimethylsiloxane) (PDMS) spacer ring with an inner diameter of ~7 mm and thickness of ~1 mm was placed on a microscope slide. The chamber was filled with ~50 μL of undiluted suspension sample and enclosed with a cover glass.

The suspensions were then centrifuged for 1 h at 3000 rpm (IEC Centra GP8R with 218 A rotor) to accelerate any potential sedimentation, and optical images and UV–vis absorbance measurements were taken again. The samples were left undisturbed for 4 days, after which centrifugation and subsequent absorbance measurements were repeated. After 1 year, the samples were centrifuged once more, and their absorbances were measured. All samples were maintained at room temperature for the duration of the experiment.

RESULTS AND DISCUSSION

Dispersions of FGSs in Aqueous SDS Solutions. Figure 2 shows optical microscopy images of FGS suspensions prepared in aqueous SDS solutions at various SDS concentrations [SDS], both a few minutes after sonication (Figure 2a) and after the samples are first centrifuged (Figure 2b). In the absence of SDS, i.e., in DI water, shortly after sonication the FGSs are aggregated in the form of ramified structures that are a few tens of micrometers in size (Figure 2a). Similar FGS structures are observed at [SDS] = 5 μM; however, in this case, the aggregates appear to be less ramified. At [SDS] = 10 μM SDS, the FGSs are aggregated in structures ~10 μm in size that appear significantly more compact than those at lower [SDS]; additionally, particles ~1 μm in size and smaller are observed. In all the samples with [SDS] > 10 μM, aggregated FGSs are absent; instead, particles that are ~1 μm and smaller are imaged. In addition to the structures described above, dark structures that are a few micrometers in size are observed in all the samples (see Supporting Information [SI], Figure S1). In contrast to the aggregates observed in DI water and in low [SDS] solutions ($\leq$ 10 μM), these dark structures appear rather dense, as indicated by their strong optical absorbance (i.e., dark color in the optical images).

After the first centrifugation, the ramified aggregates already observed in DI water prior to centrifugation are still present in suspension (Figure 2b). In the 5 μM SDS sample, the less-ramified (i.e., denser) aggregates have settled out; instead, only ramified aggregates that appear similar to those observed in DI water (presumably present before centrifugation) are observed in suspension. In the 10 μM SDS sample, the more-compact aggregates appear to have settled out, and in the samples with [SDS] $\geq$ 10 μM, the particles that are ~1 μm and smaller remain in suspension. Additionally, the dark structures with diameters of several μm that were observed in all the samples (Figure S1) are absent after centrifugation; these were likely dense FGS aggregates that could not be dispersed during the initial sonication. From the optical images of the suspensions shown in Figure 2a, we thus distinguish five types of FGS structures based on their morphologies: (i) highly ramified aggregates, (ii) less-ramified aggregates, (iii) large (> 10 μm) compact aggregates, (iv) dispersed single- or few-layer FGSs, and (v) hard aggregates a few μm in size. It is evident that, except for the hard aggregates, the morphology of the FGS structures is determined by [SDS] and thus by the extent of SDS adsorption on FGSs.

Optical images, however, only provide qualitative information about the state of dispersion in each sample, and thus, we turn to UV–vis absorbance for a quantitative analysis of the dispersion behavior. Figure 3 shows sample absorbances shortly after dispersion by sonication (blue curve) and after each centrifugation of the samples 1 h, 4 days, and 1 year later. Shortly after sonication, the absorbances of the suspensions are approximately equal (0.63 $\pm$ 0.02), confirming that approximately equal amounts of FGSs have been suspended in each sample, independent of [SDS]. Following centrifugation 1 h, 4 days, and 1 year after sonication, the absorbance in almost all the samples is decreased. The largest decrease is observed for [SDS] $\leq$ 20 μM, with a notable minimum at 10 μM that forms during the first centrifugation and deepens as a result of the second centrifugation. After centrifugation one year later, the absorbance of the DI water sample is 0.34; as [SDS] increases, the sample absorbance decreases to 0.04 at 5 μM and remains uniformly low up to 20 μM SDS, indicating that the majority of the FGSs have settled. In contrast, at [SDS] $\geq$ 40 μM, the absorbances decrease to a lesser degree. Even after a year, the average absorbance is 0.56 $\pm$ 0.07 following centrifugation, indicating that at these concentrations ~87% of the initial FGSs remain in suspension. Given the otherwise consistent trends in

dx.doi.org/10.1021/la4035326 | Langmuir XXXX, XXX, XXX–XXX

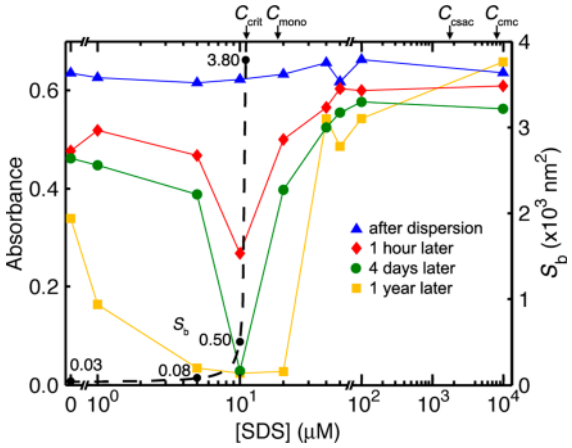

Figure 3. UV−vis absorbance of FGSs dispersed at a concentration of 0.1 mg/mL in SDS solutions with various SDS concentrations, [SDS], a few minutes after sonication (blue triangles) as well as after the first centrifugation (1 h later, red diamonds), and after centrifugation 4 days (green circles) and 1 year (orange squares) later; matching lines are drawn to guide the eye. All samples were diluted 1:9 prior to absorbance measurements. Also shown is the calculated critical overlap area for FGS aggregation S_b (dashed black line; see text for details). Indicated along the upper axis are the following: [SDS] at which SDS monolayer adsorption begins on FGSs (C_{mono}), the csac for SDS on FGSs (C_{csac}), the cmc for SDS in water (C_{cmc}), and C_{crit} (see text for description).

the data after 1 h and 4 days, the increases in absorbance at 40 μM and 10 mM after a year may be due to a disturbance of the samples or an evaporative loss of water in the intervening time. Consistent with the optical images in Figure 2, the significant decreases in absorbance for [SDS] ≤ 20 μM indicate the formation of FGS aggregates that settle out during centrifugation while the relatively high absorbances at [SDS] ≥ 40 μM suggest that in this regime FGS aggregation hardly occurs and nearly stable dispersions are obtained.

Our results show a clear relation between the settling behaviors of the different FGS structures, as measured by changes in optical absorbance, and their morphologies, as observed in the optical images. We conclude that the difference in settling behavior between ramified and compact aggregates is a result of their effective buoyant densities:[39−41] Due to their highly ramified structure, the aggregates observed in DI water have a low buoyant density and therefore do not readily sediment during centrifugation. On the other hand, the compact aggregates observed at 10 μM SDS have a higher buoyant density and thus sediment more easily during centrifugation. Accordingly, the decreases in absorbance observed for [SDS] ≤ 10 μM after centrifugation 1 h and 4 days following sonication reflect this transition from ramified to compact aggregate formation. Furthermore, at these low SDS concentrations, the large decreases in absorbance observed after a year are indicative of the rearrangement of ramified aggregates into more compact structures with time, which causes them to sediment more readily during centrifugation. Similarly, the persistent decrease in absorbance at 20 μM SDS over the course of the experiment is indicative of compact aggregate formation. In contrast, for [SDS] ≥ 40 μM, most of the FGSs are present in the form of submicrometer particles, likely representing single sheets,[1,2] and thus remain dispersed during and after centrifugation.

These observations strongly suggest that above an [SDS] of around 10−20 μM, SDS adsorption onto the FGSs provides sufficient electrostatic repulsion between the sheets to impart colloidal stability. In support of this, in the following subsection we present a theoretical model for the interaction energy between two FGSs and demonstrate that the experimentally observed transition from aggregated to colloidally stable states closely correlates with an energetic transition from a net attractive to a net repulsive regime. Additionally, in the following subsection, we demonstrate that the changes in FGS aggregate morphology correlate with changes in the sheet−sheet overlap area (dashed black curve in Figure 3, discussed below).

Modeling of the Aggregation Process. To understand the changes in FGS aggregate morphology and colloidal stability, we turn to concepts from the diffusion-limited cluster aggregation (DLCA)[42−44] and reaction-limited cluster aggregation (RLCA)[45] models. Although these models were developed for hard spherical colloidal particles, the underlying concept that changing the interaction energy between aggregating particles (by altering pH, salt concentration, or the amount of adsorbed surfactant/polymer) can profoundly affect aggregate morphology is applicable to the aggregation of flexible,[46] planar FGSs as well. For our considerations, we assume that FGS-FGS interaction is dominated by van der Waals attraction and by electrostatic repulsion from the adsorption of SDS, though hydrogen bonds may also form due to the presence of oxygen-containing functional groups. The van der Waals attraction is always present between FGSs, and its magnitude scales with sheet−sheet separation distance and overlap area.[2] Upon addition of SDS, the adsorption of anionic (i.e., electrically charged) dodecyl sulfate (DS^-) molecules onto FGSs gives rise to electrostatic repulsion between the sheets, altering their net interaction energy. The magnitude of the repulsion depends on the amount of DS^- adsorbed, the separation distance between FGSs, and the degree of sheet−sheet overlap. As the degree of overlap is an important factor to consider for platelike colloidal particles, in the following, we calculate the area-normalized interaction energy between two FGSs as a function of [SDS] and separation distance to explain the observed aggregation behavior.

We approximate FGSs as infinite parallel sheets with identical thicknesses d and calculate the interaction energy per unit area ϕ_{inter} between two FGSs as a function of separation distance h from the sum of the electrostatic energy ϕ_{elec} and the van der Waals energy ϕ_{vdW}:[47]

$$\phi_{elec} = 64 k_B T n_b \kappa^{-1} \tanh^2\left(\frac{1}{4}\psi_s\right) \times e^{(-\kappa h)} \quad (1)$$

$$\phi_{vdW} = -\frac{A}{12\pi}\left[\frac{1}{h^2} + \frac{1}{(h+2d)^2} - \frac{2}{(h+d)^2}\right] \quad (2)$$

$$\phi_{inter} = \phi_{elec} + \phi_{vdw} \quad (3)$$

Here, k_B is the Boltzmann constant, T is the temperature, n_b is the ion number density, κ^{-1} is the Debye length, ψ_s is the FGS surface potential, which can be calculated from the surface charge using the Poisson−Boltzmann equation (see SI),[47] and A is the Hamaker constant. We assume that solvation effects and hydrophobic interactions are negligible. A has been reported to lie in the range of 3×10^{-20} J for the graphite−

dx.doi.org/10.1021/la4035326 | Langmuir XXXX, XXX, XXX−XXX

water−graphite system,[48] and we use this value as an approximation for FGS−water−FGS. Though the value of A decreases with h for separations of < 2 nm,[48] for our purposes we assume that A remains constant. On the basis of previous thickness measurements by atomic force microscopy (AFM),[1,2] we take d to be 1 nm. ψ_s depends on the surface charge density, which we take to be solely due to DS^- adsorbed on FGSs and estimate from conductometric titrations of aqueous FGS suspensions,[25] assuming that FGSs in suspension have a surface area of 1850 m^2/g as reported by McAllister et al.[2] Since the material used herein came from a different batch than the FGSs used by McAllister et al.,[2] the effective surface areas may differ; however, this does not significantly affect the outcome (see SI for details on ψ_s). Additionally, to account for the steric barrier from an adsorbed SDS monolayer,[49] we assume a hard boundary at h = 1.5 nm, which is about twice the width of a hydrocarbon chain as estimated from its van der Waals radius.[50] In the following, we consider both the interaction energies and kinetics associated with transitions between the dispersed ($h \rightarrow \infty$) and aggregated (h = 1.5 nm) states for the [SDS] range in which FGS aggregation is observed. Our calculations are based only on energetics and do not include entropic effects, although we recognize that a model based on free energy minimization would be more accurate.[47,51]

We consider two parallel FGSs in suspension that approach one another with an area of overlap, S, and calculate the total interaction energy between the two FGSs as a function of h from $\phi_{total} = S \cdot \phi_{inter}$. We assume that the adsorbed surfactant is distributed homogeneously over the FGSs, and that only the overlapping areas contribute to ϕ_{total}. These are very restrictive assumptions. In reality, FGSs are flexible[46] and randomly oriented in suspension, and adsorbed SDS is not necessarily homogeneously distributed; also, edge effects likely contribute to ϕ_{total}, as Coulombic interactions decay slowly with distance. Additionally, SDS-bare regions are expected to be present on FGSs, effected by incomplete SDS adsorption onto sp^2-hybridized regions, by defects and functional groups of FGSs onto which SDS does not adsorb,[25,52] or by surfactant molecule exchange between the bulk and the surface, resulting in fluctuating coverage.[53] Consequently, the calculated energies presented in the following should not be considered as quantitatively accurate but should instead serve as order-of-magnitude estimates of general trends.

While two FGSs can interact with any S up to the value of the sheet size (~1 μm^2), we first consider an overlap area S = 100 nm^2 for the following calculations, as this yields ϕ_{total} on the order of k_BT and facilitates the discussion of concepts pertaining to aggregation kinetics. We then discuss the energetics of FGS aggregation and consider the role of S, and in particular the changes in S, in the subsequent calculations.

ϕ_{total} is plotted as a function of h in Figure 4a for three SDS concentrations: 0, 5, and 50 μM. In the following, we first describe how the energy landscape changes as a function of [SDS] and then discuss how these changes affect FGS dispersion behavior. In all cases, the total interaction energy at infinite separation, $\phi_{total,\infty}$, equals 0 (not shown in Figure 4); thus, the total interaction energy at the h = 1.5 nm steric barrier, $\phi_{total,1.5}$, represents the change in energy from infinite separation to an aggregated state. In DI water, i.e., when [SDS] = 0 μM, electrostatic repulsion between FGSs is assumed to be absent, and thus, there is no kinetic barrier for aggregation; since $\phi_{total,1.5} < 0$, there is a net attraction at the steric barrier. As [SDS] increases to 5 μM, the adsorption of SDS introduces

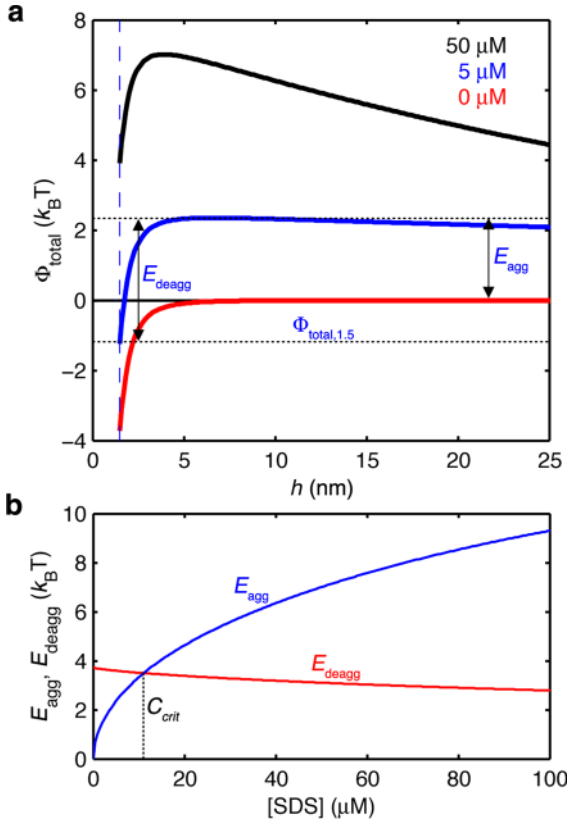

Figure 4. (a) The total interaction energy Φ_{total} (for 100 nm^2 overlap in units of k_BT) between FGSs as a function of separation distance h at SDS concentrations [SDS] of 0 μM (red), 5 μM (blue), and 50 μM (black). The dashed blue line indicates the steric barrier from adsorbed SDS at h = 1.5 nm. Indicated for the 5 μM SDS curve: the change in energy between the dispersed ($h \rightarrow \infty$) and aggregated (h = 1.5 nm) states $\Phi_{total,1.5}$, and the energy barriers for aggregation E_{agg} and deaggregation E_{deagg}. (b) The dependence of E_{agg} and E_{deagg} on [SDS]. The critical SDS concentration C_{crit} at which the barriers are equal is indicated. All energies were calculated assuming an overlap area S = 100 nm^2.

electrostatic repulsion between FGSs, creating a barrier for aggregation, E_{agg}; the energy barrier for deaggregation E_{deagg}, however, is larger as $E_{deagg} = E_{agg} - \phi_{total,1.5}$. Increasing [SDS] to 50 μM, electrostatic repulsion from adsorbed SDS causes E_{agg} to exceed E_{deagg} as $\phi_{total,1.5} > 0$; now, there is a net repulsion at the steric barrier. To further illustrate the influence of SDS adsorption on the energy landscape between two FGSs, in Figure 4b we show the dependence of E_{agg} and E_{deagg} on [SDS]. We note that at a critical SDS concentration of $C_{crit} \approx 11$ μM, E_{agg} and E_{deagg} are equal to one another, and $\phi_{total,1.5} = 0$. Thus, C_{crit} signifies a transition from a net attractive to a net repulsive regime and, as demonstrated below, also indicates the transtion from persistently aggregated states to stably dispersed suspensions.

In the absence of external energy input (e.g., from ultrasonication or shear flow), FGSs will aggregate only if the thermal energy is strong enough for FGSs to overcome E_{agg}. To determine if an aggregated state will persist, we consider variations in the rate of aggregation versus the rate of deaggregation, as done in previous studies of aggregation transitions.[44,54−57] The basic concept is that systems will evolve toward a persistently aggregated state only if the rate of aggregation, $r_{agg} \propto \exp[-E_{agg}/(k_BT)]$,[54−57] exceeds the rate of

dx.doi.org/10.1021/la4035326 | Langmuir XXXX, XXX, XXX−XXX

deaggregation, $r_{deagg} \propto \exp[-E_{deagg}/(k_BT)]$.[54−57] Thus at 0 μM SDS, $r_{agg} \gg r_{deagg}$ as $E_{agg} = 0$ and the sticking probability for colliding FGSs, which can be expressed simplistically as $\sigma = (1 + r_{deagg}/r_{agg})^{-1}$,[55,57] is assumed to be close to 1, implying that FGSs aggregate upon contact. Indeed, the highly ramified aggregates observed in DI water (Figure 2a) are reminiscent of the ramified structures that form when initially dispersed spherical colloids aggregate in the absence of interparticle repulsion, as described by modified versions of the DLCA model.[44,58] This suggests that even in the absence of SDS, the FGSs were in a dispersed state during and immediately after sonication, and that the highly ramified structures formed through reaggregation of initially dispersed FGSs.

As [SDS] increases to 5 μM, E_{agg} grows relative to E_{deagg}, causing σ to decrease; thus, colliding FGSs do not always remain aggregated and can restructure toward denser states.[44] The less-ramified aggregates observed at 5 μM SDS (Figure 2a) are remeniscent of decreased branching that occurs when there is a finite probability that thermal energy can cause primary particles to repeatedly aggregate and deaggregate;[62] this enables aggregate restructuring via an increase in the overlap area S, as discussed below.[44,58] As [SDS] increases to C_{crit}, r_{agg} approaches r_{deagg} since E_{agg} approaches E_{deagg}. The compact aggregates observed at 10 μM (Figure 2a), i.e., at an [SDS] close to our estimate of C_{crit}, resemble the aggregation of initially dispersed spherical colloids into compact structures under conditions in which the two energy barriers are nearly equal.[44,58] Furthermore, as $\sigma \approx 0.5$ at C_{crit}, the likelihood of aggregate restructuring is at a maximum.

As [SDS] exceeds C_{crit}, $\phi_{total,1.5}$ becomes positive, and E_{agg} is now greater than E_{deagg}; thus, r_{deagg} exceeds r_{agg}, and σ approaches zero. From a kinetics point of view, we therefore take C_{crit} to be the onset of the transition from persistently aggregated states to stably dispersed suspensions. For comparison, C_{crit} is indicated on the upper axis in Figure 3 along with the value of [SDS] at which the adsorbed surfactant monolayer reaches full coverage on FGSs ($C_{mono} \approx 18$ μM),[25] the csac for SDS on FGSs ($C_{csac} \approx 1.8$ mM),[25] and the cmc for SDS in water ($C_{cmc} \approx 8.1$ mM).[35−37]

Turning now to the energetics of FGS aggregation, for negative values of $\phi_{total,1.5}$ a binding energy $E_b = -\phi_{total,1.5}$ can be defined. While FGSs in suspension have a Maxwell−Boltzmann thermal energy distribution, we first consider a constant E_b on the order of k_BT to gain insight on the role of S in FGS aggregation. For [SDS] < C_{crit}, i.e., when $\phi_{total,1.5} < 0$ and stable aggregates are expected to form, we calculate the critical overlap area S_b that results in $E_b = k_BT$ (Figure 3, dashed black line). Conceptually, at a given [SDS], S_b is the minimum overlap area that FGSs with thermal energy k_BT must collide with for aggregation to occur (i.e., $E_b > k_BT$ when $S > S_b$). We note that changing E_b in this calculation simply scales S_b proportionally, leaving the curve qualitatively unchanged. At 0 μM SDS, $S_b \approx 30$ nm^2 and as [SDS] increases toward C_{crit}, S_b increases to ∼500 nm^2 at 10 μM then rises dramatically to ∼3800 nm^2 at 10.9 μM. Based on our calculation of S_b, as [SDS] increases and E_b decreases, a larger degree of FGS overlap is expected, which is consistent with the increasingly compact aggregate structures observed in Figure 2 and corroborates the analysis of Figure 4 discussed above. Accordingly, as settling behavior changes with aggregate morphology,[39−41] the decrease in UV−vis absorbance observed as [SDS] increases from zero to C_{crit} after the first centrifugation (Figure 3) reflects the transition from ramified to compact aggregate formation.

Due to the thermal energy distribution, however, random thermal fluctuations may be large enough for aggregated FGSs to overcome E_{deagg}, enabling them to restructure by changing S. We note that a decrease in S results in a smaller E_{deagg} and thus a higher r_{deagg}; conversely, aggregates with a larger S have a lower r_{deagg} and are more likely to survive. Furthermore, as systems tend toward their lowest-energy state, at a given [SDS] there is also an energetic driving force for aggregated FGSs to restructure by increasing S and forming more compact structures, as this acts to decrease $\phi_{total,1.5}$ (i.e., increase E_b). Indeed, the progressive decrease in absorbance that is observed for [SDS] < C_{crit} (Figure 3) is indicative of the rearrangement of ramified aggregates into more compact structures on a time scale of days (for [SDS] → C_{crit}) through months (for [SDS] → 0), enabling them to sediment during subsequent centrifugations. Although aggregate restructuring via an increase in S is unique to sheetlike particles (as spheres only make point contacts), it is analogous to the restructuring of hard spherical colloids via an increase in coordination number.[46]

At values of [SDS] slightly above C_{crit} (but < 40 μM), the decrease in UV−vis absorbance over time (Figure 3) implies that persistent FGS aggregation does occur, though the rate appears to decrease as [SDS] increases. This observation conflicts with the positive $\phi_{total,1.5}$ values calculated for this [SDS] range, and the discrepancy may be due to the approximations in our model, as discussed below. At [SDS] ≥ 40 μM, while the decrease in average absorbance following the first centrifugation is attributed to the settling of hard aggregates, after the second centrifugation the average absorbance decreases slightly further. This is possibly due to a small degree of FGS reaggregation, however it is most likely due to the settling of hard aggregates that did not sediment during the first centrifugation. Indeed, after a year the average absorbance does not decrease further by an appreciable amount, especially considering the large drop in absorbance observed after a year for [SDS] < 40 μM, suggesting that no further reaggregation occurred.

While it is striking that our calculated value of C_{crit} lies close to the experimentally observed minimum in the absorbance and appears to mark the transition from the aggregated structures to the dispersed state, we are cautious not to overinterpret this correlation. Due to the many assumptions and approximations that were made, our calculations of ϕ_{inter}, ϕ_{total}, and S_b are not quantitatively accurate. As such, one possible explanation for FGS aggregation above C_{crit} is that our calculated value of ∼11 μM SDS for the critical concentration is too low and that the transition from negative to positive $\phi_{total,1.5}$ actually occurs at a higher [SDS]. Another possible explanation could be that at [SDS] between C_{crit} and 40 μM, thermal energy may be able to overcome the increase in energy associated with aggregation, as the magnitudes of both $\phi_{total,1.5}$ and E_{agg} are on the order of k_BT. In particular, considering that FGSs are flexible and also could initially aggregate in more geometrically complex configurations than considered here (e.g., edge on plane), it is plausible that kinetically trapped aggregates may form. At [SDS] ≥ 40 μM, though, as $\phi_{total,1.5}$ grows increasingly positive and $E_{agg} \gg k_BT$, aggregation is likely prevented both energetically and kinetically, such that dispersed FGSs are electrostatically stabilized.

dx.doi.org/10.1021/la4035326 | Langmuir XXXX, XXX, XXX−XXX

CONCLUSION

We have shown that SDS concentrations ≥ 40 μM, i.e., above the onset of monolayer adsorption on FGSs, are sufficient to achieve colloidal stability in aqueous FGS dispersions. Using optical microscopy and UV−vis absorbance measurements in conjunction with a simple interaction energy model, we demonstrated the influence of SDS adsorption on the aggregation of platelike FGSs and found that aggregate morphology (and thus settling behavior) depends strongly on SDS concentration: In the absence of the surfactant, due to the lack of electrostatic repulsion, van der Waals attraction dominates and causes FGSs to form highly ramified aggregates. As the SDS concentration is increased, the growing repulsion from adsorbed SDS causes FGS aggregates to develop a more compact structure due to an increase in sheet−sheet overlap area. Additionally, over time, ramified FGS aggregates restructure into more compact structures via an increase in the overlap area. Above a critical SDS concentration, we find that the dispersed state becomes increasingly stabilized, and the growing kinetic barrier eventually prevents the reaggregation of FGSs for at least a year. Finally, while the formation of stable dispersions of FGSs in aqueous media is important for many applications such as the processing of graphene−metal oxide nanocomposites, graphene−polymer composites, and high surface area tapes, we do not assume that a well-dispersed state is always optimal. Certainly, for applications in which control of FGS aggregate morphology is desired, the findings presented herein are relevant.

ASSOCIATED CONTENT

Supporting Information

Optical images of hard aggregates and details regarding the influence of FGS surface area on the calculations. This material is available free of charge via the Internet at http://pubs.acs.org.

AUTHOR INFORMATION

Corresponding Author

*E-mail: iaksay@princeton.edu. Telephone: 609-258-4393.

Notes

The authors declare no competing financial interest.

ACKNOWLEDGMENTS

This work was supported by the Pacific Northwest National Laboratory (operated for the United States Department of Energy by Battelle) under Grant Number DE-AC05-76RL01830.

REFERENCES

(1) Schniepp, H. C.; Li, J.-L.; McAllister, M. J.; Sai, H.; Herrera-Alonso, M.; Adamson, D. H.; Prud'homme, R. K.; Car, R.; Saville, D. A.; Aksay, I. A. Functionalized Single Graphene Sheets Derived from Splitting Graphite Oxide. *J. Phys. Chem. B* **2006**, *110*, 8535−8539.

(2) McAllister, M. J.; Li, J.-L.; Adamson, D. H.; Schniepp, H. C.; Abdala, A. A.; Liu, J.; Herrera-Alonso, M.; Milius, D. L.; Car, R.; Prud'homme, R. K.; Aksay, I. A. Single Sheet Functionalized Graphene by Oxidation and Thermal Expansion of Graphite. *Chem. Mater.* **2007**, *19*, 4396−4404.

(3) Stankovich, S.; Piner, R. D.; Chen, X.; Wu, N.; Nguyen, S. T.; Ruoff, R. S. Stable Aqueous Dispersions of Graphitic Nanoplatelets via the Reduction of Exfoliated Graphite Oxide in the Presence of Poly(Sodium 4-Styrenesulfonate). *J. Mater. Chem.* **2006**, *16*, 155−158.

(4) Wang, D.; Choi, D.; Li, J.; Yang, Z.; Nie, Z.; Kou, R.; Hu, D.; Wang, C.; Saraf, L. V.; Zhang, J.; Aksay, I. A.; Liu, J. Self-Assembled TiO_2−Graphene Hybrid Nanostructures for Enhanced Li-Ion Insertion. *ACS Nano* **2009**, *3*, 907−914.

(5) Wu, Z.-S.; Ren, W.; Wen, L.; Gao, L.; Zhao, J.; Chen, Z.; Zhou, G.; Li, F.; Cheng, H.-M. Graphene Anchored with CO_3O_4 Nanoparticles as Anode of Lithium Ion Batteries with Enhanced Reversible Capacity and Cyclic Performance. *ACS Nano* **2010**, *4*, 3187−3194.

(6) Wang, D.; Kou, R.; Choi, D.; Yang, Z.; Nie, Z.; Li, J.; Saraf, L. V.; Hu, D.; Zhang, J.; Graff, G. L.; Liu, J.; Pope, M. A.; Aksay, I. A. Ternary Self-Assembly of Ordered Metal Oxide−Graphene Nanocomposites for Electrochemical Energy Storage. *ACS Nano* **2010**, *4*, 1587−1595.

(7) Zhu, X.; Zhu, Y.; Murali, S.; Stoller, M. D.; Ruoff, R. S. Nanostructured Reduced Graphene Oxide/Fe_2O_3 Composite as a High-Performance Anode Material for Lithium Ion Batteries. *ACS Nano* **2011**, *5*, 3333−3338.

(8) Wang, J. C.; Wang, X. B.; Xu, C. H.; Zhang, M.; Shang, X. P. Preparation of Graphene/Poly(Vinyl Alcohol) Nanocomposites with Enhanced Mechanical Properties and Water Resistance. *Polym. Int.* **2011**, *60*, 816−822.

(9) Bao, C. L.; Guo, Y. Q.; Song, L.; Hu, Y. Poly(Vinyl Alcohol) Nanocomposites Based on Graphene and Graphite Oxide: A Comparative Investigation of Property and Mechanism. *J. Mater. Chem.* **2011**, *21*, 13942−13950.

(10) Ozbas, B.; O'Neill, C. D.; Register, R. A.; Aksay, I. A.; Prud'homme, R. K.; Adamson, D. H. Multifunctional Elastomer Nanocomposites with Functionalized Graphene Single Sheets. *J. Polym. Sci., Part B: Polym. Phys.* **2012**, *50*, 910−916.

(11) Verdejo, R.; Barroso-Bujans, F.; Rodriguez-Perez, M. A.; de Saja, J. A.; Lopez-Manchado, M. A. Functionalized Graphene Sheet Filled Silicone Foam Nanocomposites. *J. Mater. Chem.* **2008**, *18*, 2221−2226.

(12) Stankovich, S.; Dikin, D. A.; Dommett, G. H. B.; Kohlhaas, K. M.; Zimney, E. J.; Stach, E. A.; Piner, R. D.; Nguyen, S. T.; Ruoff, R. S. Graphene-Based Composite Materials. *Nature* **2006**, *442*, 282−286.

(13) Sabourin, J. L.; Dabbs, D. M.; Yetter, R. A.; Dryer, F. L.; Aksay, I. A. Functionalized Graphene Sheet Colloids for Enhanced Fuel/Propellant Combustion. *ACS Nano* **2009**, *3*, 3945−3954.

(14) Liu, L. M.; Car, R.; Selloni, A.; Dabbs, D. M.; Aksay, I. A.; Yetter, R. A. Enhanced Thermal Decomposition of Nitromethane on Functionalized Graphene Sheets: *ab initio* Molecular Dynamics Simulations. *J. Am. Chem. Soc.* **2012**, *134*, 19011−19016.

(15) Bagri, A.; Mattevi, C.; Acik, M.; Chabal, Y. J.; Chhowalla, M.; Shenoy, V. B. Structural Evolution During the Reduction of Chemically Derived Graphene Oxide. *Nat. Chem.* **2010**, *2*, 581−587.

(16) Coleman, J. N. Liquid-Phase Exfoliation of Nanotubes and Graphene. *Adv. Funct. Mater.* **2009**, *19*, 3680−3695.

(17) Villar-Rodil, S.; Paredes, J. I.; Martínez-Alonso, A.; Tascón, J. M. D. Preparation of Graphene Dispersions and Graphene-Polymer Composites in Organic Media. *J. Mater. Chem.* **2009**, *19*, 3591−3593.

(18) Pham, V. H.; Dang, T. T.; Cuong, T. V.; Hur, S. H.; Kong, B. S.; Kim, E. J.; Chung, J. S. Synthesis of Highly Concentrated Suspension of Chemically Converted Graphene in Organic Solvents: Effect of Temperature on the Extent of Reduction and Dispersibility. *Korean J. Chem. Eng.* **2012**, *29*, 1−6.

(19) Korkut, S.; Roy-Mayhew, J. D.; Dabbs, D. M.; Milius, D. L.; Aksay, I. A. High Surface Area Tapes Produced with Functionalized Graphene. *ACS Nano* **2011**, *5*, 5214−5222.

(20) Daimon, M.; Masumura, A. Measurement of the Refractive Index of Distilled Water from the Near-Infrared Region to the Ultraviolet Region. *Appl. Opt.* **2007**, *46*, 3811−3820.

(21) Jung, I.; Vaupel, M.; Pelton, M.; Piner, R.; Dikin, D. A.; Stankovich, S.; An, J.; Ruoff, R. S. Characterization of Thermally Reduced Graphene Oxide by Imaging Ellipsometry. *J. Phys. Chem. C* **2008**, *112*, 8499−8506.

(22) Yang, D.; Velamakanni, A.; Bozoklu, G.; Park, S.; Stoller, M.; Piner, R. D.; Stankovich, S.; Jung, I.; Field, D. A.; Ventrice, C. A., Jr. Chemical Analysis of Graphene Oxide Films after Heat and Chemical Treatments by X-Ray Photoelectron and Micro-Raman Spectroscopy. *Carbon* **2009**, *47*, 145−152.

(23) Konkena, B.; Vasudevan, S. Understanding Aqueous Dispersibility of Graphene Oxide and Reduced Graphene Oxide through pK_a Measurements. *J. Phys. Chem. Lett.* **2012**, *3*, 867−872.
(24) Li, D.; Müller, M. B.; Gilje, S.; Kaner, R. B.; Wallace, G. G. Processable Aqueous Dispersions of Graphene Nanosheets. *Nat. Nanotechnol.* **2008**, *3*, 101−105.
(25) Hsieh, A.; Punckt, C.; Korkut, S.; Aksay, I. A. Adsorption of Sodium Dodecyl Sulfate on Functionalized Graphene Measured by Conductometric Titration. *J. Phys. Chem. B* **2013**, *117*, 7950−7958.
(26) Greenwood, F, G.; Parfitt, G, D.; Picton, N, H.; Wharton, D, G., Adsorption and Wetting Phenomena Associated with Graphon in Aqueous Surfactant Solutions. In *Adsorption from Aqueous Solution*, American Chemical Society: 1968; Vol. *79*, pp 135−144.
(27) Kawasaki, H.; Ban, K.; Maeda, H. Investigation of the Stability of Graphite Particle Dispersion and the Hemimicelle Formation Process at Graphite/Solution Interfaces Using Atomic Force Microscopy. *J. Phys. Chem. B* **2004**, *108*, 16746−16752.
(28) Lotya, M.; Hernandez, Y.; King, P. J.; Smith, R. J.; Nicolosi, V.; Karlsson, L. S.; Blighe, F. M.; De, S.; Wang, Z.; McGovern, I. Liquid Phase Production of Graphene by Exfoliation of Graphite in Surfactant/Water Solutions. *J. Am. Chem. Soc.* **2009**, *131*, 3611−3620.
(29) Green, A. A.; Hersam, M. C. Solution Phase Production of Graphene with Controlled Thickness via Density Differentiation. *Nano Lett.* **2009**, *9*, 4031−4036.
(30) Smith, R. J.; Lotya, M.; Coleman, J. N. The Importance of Repulsive Potential Barriers for the Dispersion of Graphene Using Surfactants. *New J. Phys.* **2010**, *12*, 125008.
(31) Fernández-Merino, M. J.; Paredes, J.; Villar-Rodil, S.; Guardia, L.; Solís-Fernández, P.; Salinas-Torres, D.; Cazorla-Amorós, D.; Morallón, E.; Martínez-Alonso, A.; Tascón, J. Investigating the Influence of Surfactants on the Stabilization of Aqueous Reduced Graphene Oxide Dispersions and the Characteristics of Their Composite Films. *Carbon* **2012**, *50*, 3184−3194.
(32) Pu, N. W.; Wang, C. A.; Liu, Y. M.; Sung, Y.; Wang, D. S.; Ger, M. D. Dispersion of Graphene in Aqueous Solutions with Different Types of Surfactants and the Production of Graphene Films by Spray or Drop Coating. *J. Taiwan Inst. Chem. Eng.* **2012**, *43*, 140−146.
(33) Staudenmaier, L. Verfahren zur Darstellung der Graphitsäure. *Ber. Dtsch. Chem. Ges.* **1898**, *31*, 1481−1487.
(34) Brunauer, S.; Emmett, P. H.; Teller, E. Adsorption of Gases in Multimolecular Layers. *J. Am. Chem. Soc.* **1938**, *60*, 309−319.
(35) Williams, R.; Phillips, J.; Mysels, K. The Critical Micelle Concentration of Sodium Lauryl Sulphate at 25 °C. *Trans. Faraday Soc.* **1955**, *51*, 728−737.
(36) Anghel, D.; Ciocan, N. Critical Micelle Concentration (CMC) Determination with the Aid of Liquid Membrane Electrode Sensitive to Dodecyl Sulfate Anion. *Colloid Polym. Sci.* **1976**, *254*, 114−115.
(37) Newbery, J.; Smith, V. Measurement of the Critical Micelle Concentration by Ion-Selective Electrodes. *Colloid Polym. Sci.* **1978**, *256*, 494−495.
(38) Hernandez, Y.; Nicolosi, V.; Lotya, M.; Blighe, F. M.; Sun, Z.; De, S.; McGovern, I.; Holland, B.; Byrne, M.; Gun'Ko, Y. K. High-Yield Production of Graphene by Liquid-Phase Exfoliation of Graphite. *Nat. Nanotechnol.* **2008**, *3*, 563−568.
(39) Li, D. H.; Ganczarczyk, J. Fractal Geometry of Particle Aggregates Generated in Water and Wastewater Treatment Processes. *Environ. Sci. Technol.* **1989**, *23*, 1385−1389.
(40) Gregory, J. The Role of Floc Density in Solid-Liquid Separation. *Filtr. Sep.* **1998**, *35*, 367−371.
(41) Khelifa, A.; Hill, P. S. Models for Effective Density and Settling Velocity of Flocs. *J. Hydraul. Res.* **2006**, *44*, 390−401.
(42) Meakin, P. Formation of Fractal Clusters and Networks by Irreversible Diffusion-Limited Aggregation. *Phys. Rev. Lett.* **1983**, *51*, 1119−1122.
(43) Kolb, M.; Botet, R.; Jullien, R. Scaling of Kinetically Growing Clusters. *Phys. Rev. Lett.* **1983**, *51*, 1123−1126.
(44) Shih, W. Y.; Aksay, I. A.; Kikuchi, R. Reversible-Growth Model: Cluster-Cluster Aggregation with Finite Binding Energies. *Phys. Rev. A* **1987**, *36*, 5015−5019.
(45) Kolb, M.; Jullien, R. Chemically Limited Versus Diffusion Limited Aggregation. *J. Phys. (Paris), Lett.* **1984**, *45*, 977−981.
(46) Schniepp, H. C.; Kudin, K. N.; Li, J.-L.; Prud'homme, R. K.; Car, R.; Saville, D. A.; Aksay, I. A. Bending Properties of Single Functionalized Graphene Sheets Probed by Atomic Force Microscopy. *ACS Nano* **2008**, *2*, 2577−2584.
(47) Russel, W. B.; Saville, D. A.; Schowalter, W. R., *Colloidal Dispersions*. Cambridge University Press: 1992.
(48) Li, J. L.; Chun, J.; Wingreen, N. S.; Car, R.; Aksay, I. A.; Saville, D. A. Use of Dielectric Functions in the Theory of Dispersion Forces. *Phys. Rev. B* **2005**, *71*, 235412.
(49) Overbeek, J. T. G. Recent Developments in the Understanding of Colloid Stability. *J. Colloid Interface Sci.* **1977**, *58*, 408−422.
(50) Bondi, A. van der Waals Volumes and Radii. *J. Phys. Chem.* **1964**, *68*, 441−451.
(51) Shih, W. Y.; Aksay, I. A.; Kikuchi, R. Phase Diagrams of Charged Colloidal Particles. *J. Chem. Phys.* **1987**, *86*, 5127−5132.
(52) Glover, A. J.; Adamson, D. H.; Schniepp, H. C. Charge-Driven Selective Adsorption of Sodium Dodecyl Sulfate on Graphene Oxide Visualized by Atomic Force Microscopy. *J. Phys. Chem. C* **2012**, *116*, 20080−20085.
(53) Saville, D. A.; Chun, J.; Li, J. L.; Schniepp, H. C.; Car, R.; Aksay, I. A. Orientational Order of Molecular Assemblies on Inorganic Crystals. *Phys. Rev. Lett.* **2006**, *96*, 018301.
(54) Langmuir, I. The Vapor Pressure of Metallic Tungsten. *Phys. Rev.* **1913**, *2*, 329−342.
(55) Langmuir, I. The Constitution and Fundamental Properties of Solids and Liquids. Part I. Solids. *J. Am. Chem. Soc.* **1916**, *38*, 2221−2295.
(56) Verwey, E. J. W.; Overbeek, J. T. G.; van Nes, K., *Theory of the Stability of Lyophobic Colloids: The Interaction of Sol Particles Having an Electric Double Layer*; Elsevier: New York: 1948.
(57) Ehrlich, G. On the Kinetics of Chemisorption. *J. Phys. Chem.* **1955**, *59*, 473−477.
(58) Liu, J.; Shih, W. Y.; Sarikaya, M.; Aksay, I. A. Fractal Colloidal Aggregates with Finite Interparticle Interactions: Energy Dependence of the Fractal Dimension. *Phys. Rev. A* **1990**, *41*, 3206−3213.